THE JOURNAL OF PHYSICAL CHEMISTRY C

Article

Cite This: J. Phys. Chem. C 2018, 122, 8573−8580

pubs.acs.org/JPCC

Effect of Surface Passivation on Nanodiamond Crystallinity

Ryan A. Beck,[†,§] Alessio Petrone,[†,§] Joseph M. Kasper,[†] Matthew J. Crane,[‡] Peter J. Pauzauskie,[‡] and Xiaosong Li*[,†]

[†]Department of Chemistry and [‡]Department of Materials Science and Engineering, University of Washington, Seattle, Washington 98195, United States

Supporting Information

ABSTRACT: Diamonds approaching the nanoscale have the potential for use as probe materials as their optical properties can be sensitive to optical/electric fields, mechanical stress/pressure, and the configuration of nuclear spins. The surface of nanodiamonds impacts their optical properties and sensing capabilities, and examining the nanodiamond surface through X-ray absorption can give insights into molecular surface structures. Here, quantum dot models with varying amounts of surface carbon passivation are prepared, optimized, and compared. The loss of the diamond sp^3 lattice is examined by investigating the bond length and tetrahedral character of the carbons comprising nanodiamonds for the appearance of aromatic sp^2 surface domains. Electronic transitions in the carbon K-edge region, using the energy-specific time-dependent density functional theory method, as well as vibrational spectra are computed from the optimized models. The surface reorganization is shown to affect the electronic characteristics of the nanodiamond. As a result, there is a distinct absorption peak in the carbon K-edge region, along with stretching modes in the vibrational spectra, that can be correlated to the nature of the surface hybridization of the nanodiamond.

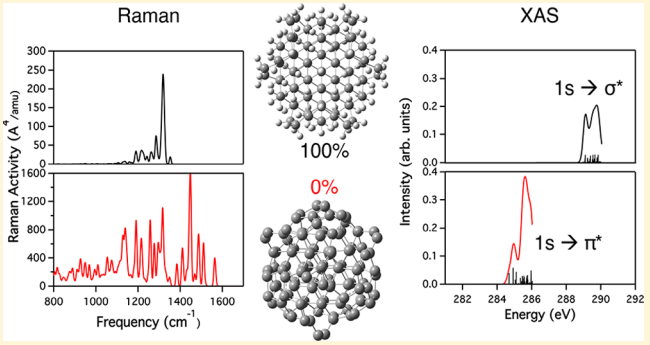

INTRODUCTION

Nanodiamonds are interesting materials due to their stability and potential for use in biological imaging, quantum computing, drug delivery, and sensing as a result of their lack of photobleaching, spin-polarized photoluminescense, and long spin lifetimes when doped.[1−9] Bulk, undoped diamonds are insulators with a band gap of approximately 5.5 eV.[10] They are thus transparent to visible radiation; however, dopants such as the nitrogen vacancy and silicon split divacancy can lead to optical signatures in the visible region.[1,11−13] These optical signatures can be tuned by altering the size of the nanocrystal. As the size of the nanocrystal decreases, discrete electronic states emerge at the band edges along with an energetic increment of the band gap as a result of the quantum confinement effect.[7,14−22]

In diamond, carbon is arranged into a highly symmetric, tetrahedral sp^3 lattice. However, because of graphitic pre-edge features that appear in the carbon K-edge energy region of X-ray and electron energy loss spectroscopy of nanodiamonds, it has been theorized that as diamond approaches the nanoscale the surface carbons arrange to form sp^2 features.[2,13,23,24] Earlier theories on the arrangement of the carbons predicted a diamond core with a graphitic shell around it.[1,25] This model for describing the surface of the diamond still cannot describe an experimentally determined deviation from perfect lattice Bragg peaks.[25] Thus, an improved model was proposed where nanodiamonds arrange themselves in a manner similar to that in Figure 1.[1,25] In this model, there is an sp^3 diamond core surrounded by a shell of sp^3 carbon atoms where the diamond lattice deviates from its perfect tetrahedral arrangement, labeled S_2 in the figure. Finally, this intermediate shell interacts with the graphitic, sp^2 surface layer, labeled S_1 in the figure.[25]

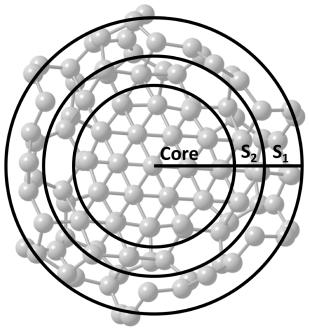

Figure 1. Proposed model for nanodiamond surface reorganization composed of a diamond lattice core, a layer of sp^3 carbon where the diamond lattice deteriorates (S_2), and the surface (S_1).[1,25]

Surface rearrangement, and thus the carbon hybridization, of nanodiamonds has been used to describe experimentally determined features on optical spectra, such as the carbon X-ray absorption 285 eV pre-edge.[2,13,23,26] In the past few years,

Received: January 12, 2018
Revised: March 8, 2018
Published: April 4, 2018

DOI: 10.1021/acs.jpcc.8b00354
J. Phys. Chem. C 2018, 122, 8573−8580

the effects of surface passivation, symmetry, and functionalization on the diamond lattice reorganization have also been studied computationally.[27−31] However, a detailed understanding of the interplay between the surface rearrangement (i.e., sp^2 moieties, graphitic and sp^3 strained layers) and the presence of localized defects in the lattice (i.e., dopants)[25] on the pre-edge features that appear in the carbon K-edge energy region of the X-ray absorbance spectrum has still not been fully accomplished.

Thus, in this study the effects of different surface hybridizations on the Raman scattering vibrational spectroscopy and X-ray absorption are examined using a finite cluster approach combined with harmonic treatment and energy-specific time-dependent density functional theory (TDDFT),[32−34] respectively. This technique has shown very promising results for the theoretical characterization of both the excited electronic states of defect-containing semiconductor clusters and light elements[11,33,35−40] and the vibrational/dynamical properties of molecules.[39,41−45] Rearrangement of the surface carbon hybridization is predicted through the structural response to different surface passivations. Hydrogen was chosen to passivate the surface carbon dangling bonds, given that hydrogen surface termination can be realized experimentally using a hydrogen plasma process.[1,46,47] Other moieties such as those containing oxygen and nitrogen are commonly found on the surface as a byproduct of the manufacturing and purification methods including the detonation of high explosives, a high-pressure, high-temperature multianvil press, and, most recently, laser-heated diamond anvil cells (LH-DAC).[1,13,48,49] The unique use of noble gas pressure media during LH-DAC processing maximizes the probability of graphitic surface reconstruction.

In this work, density functional theory calculations are used with a cluster approach to find the optimized molecular geometry for the structures of varying surface passivations, as shown in Figure 2. This level of theory has already been used

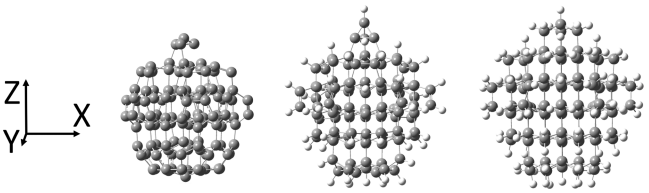

Figure 2. From left to right, B3LYP/6-31G(d)-optimized $C_{121}H_0$, $C_{121}H_{58}$, and $C_{121}H_{104}$ diamond structures.

effectively to study nitrogen-doped nanodiamonds of similar dimensions.[11] To validate the predicted structural reorganization, infrared and Raman spectra have been calculated on systems with various degrees of surface passivation and compared with the experiments. The origins of the carbon K-edge pre-edge feature motivated the study of the X-ray absorption spectroscopy (XAS) in this energy region. XAS is elementally specific with large separations between the responses for different elements and gives information about weakly bound states to which it excites. Therefore, information about the surface hybridization can be determined through XAS.[50] Since the molecular origin of the X-ray pre-edge feature for nanodiamonds is not fully understood, this theoretical study is motivated by a desire to understand the relationship between this feature and the surface arrangement in nanodiamonds.

METHODOLOGY

Nanodiamonds were constructed to be nearly spherical with a bulk fcc lattice parameter of a = 0.357 nm[10] according to the procedure presented in ref 11. Hydrogen atoms were used to passivate the surface carbon atoms and to saturate surface dangling bonds. Although other moieties are generally present on the surface, chemical treatments of the surface can provide a more uniform passivation.[1] Before hydrogen removal or optimization, the diamonds have C_{3v} symmetry, and two sizes, ∼1.4 nm ($C_{182}H_{142}$) and ∼1.2 nm ($C_{121}H_{104}$) in diameter, have been used throughout the article. These systems are similar, but slightly smaller, than commercially available nanodiamonds from laser-heated diamond anvil cell synthesis or detonation synthesis.[1,13,48] Given that the Bohr exciton radius for diamond is ∼1.6 nm,[51] the electronic properties of these diamond clusters are expected to exhibit quantum confinement effects.[11]

Calculations were preformed using the Gaussian[52] electronic structure software package. The ground-state electronic structures were obtained by solving the Kohn−Sham equation using the hybrid Becke, three-parameter, Lee−Yang−Parr (B3LYP) functional[53−55] with a 6-31g(d) basis. The theory level employed has been previously validated for the description of the electronic structure and optical properties of both pure and nitrogen-vacancy-doped diamonds of the same dimensions.[11] To examine the effects of the surface passivation on the diamond lattice as the surface becomes more unsaturated, hydrogens were removed from the surface and the resulting structure was fully optimized.[56] This surface reorganization is analogous to what has been hypothesized to occur when nanodiamonds are synthesized within a laser-heated diamond anvil cell that uses a noble gas (i.e., neon or argon) as the nearly hydrostatic pressure medium.[13] Hydrogens were removed in such a way as to preserve the symmetry of the unoptimized structures and to obtain a homogeneous hydrogen density across the surface of the nanodiamond (Figure 2).

To verify the structures returned from the optimization were true minima and to compute the vibrational frequencies, the second derivatives of the energy with respect to the Cartesian nuclear coordinates were calculated. Given the number of atoms and possible arrangements of the systems studied, there are several structures with similar bonding structures and degenerate energies that can result from the optimizations. To ensure that the optimized structures represent physically valid models, XAS and Raman vibrational spectra were computed and compared to the experimental results. In addition, a detailed analysis of the surface reorganization is presented, providing a comparison with previous computational studies on diamonds of similar sizes.[2,30,31] The average computed properties over each optimized nanodiamond structure are similar and representative of the experimental data, suggesting that the results presented herein are valid.

The XAS was calculated using time-dependent density functional theory (TDDFT) within the linear-response framework[57−59] and its energy-specific implementation for high-energy states[32−34] for the differently passivated nanodiamonds. The carbon K-edge was calculated, with a convergence of 1×10^{-3} eV on the energy, to determine the effect of the surface hybridization on the resulting response. The XAS K-edge spectra were calculated with the 1.2 nm diamond due to its reduced computational cost, in comparison to the 1.4 nm nanodiamond. The 1.2 nm nanodiamond model is shown to be

DOI: 10.1021/acs.jpcc.8b00354
J. Phys. Chem. C 2018, 122, 8573−8580

of an appropriate size to capture the surface reorganization by comparing its structure reorganization with the corresponding 1.4 nm nanodiamond model. The resulting transitions were uniformly shifted[33] by 12 eV (Table S1 for a detailed comparison) in all discussions, reported spectra, and tables so as to better compare with experimentally obtained results for the onset of the pure bulk diamond carbon K-edge obtained with both electron energy loss spectroscopy[3,30] and XAS.[2,23]

To compare the amount of tetrahedral character exhibited by different diamond atoms within the core and surface of a nanodiamond and between nanodiamonds with different levels of surface passivation, the average carbon−carbon bond distance at different distances from the origin of the nanodiamond was examined. The average deviation from an ideal tetrahedral bond angle (109.5°) subtended at each carbon center was examined in addition to the bond length to show either the existence of a tetrahedral lattice or the degradation of the lattice. Three surface passivations were analyzed for the 1.2 nm nanodiamond, where the surface has 0 (no hydrogens), 50, and 100% (all surface dangling bonds are passivated by hydrogens) of the original hydrogen passivation.

RESULTS AND DISCUSSION

Structural Reorganization. The lattice structural reorganization and resulting surface layouts are summarized as functions of the different degrees of hydrogen passivation (0, 50, and 100%) in Figure 3, where the average bond length (top panels) and bond angle deviation (bottom panels) are shown. An overall lattice strain, a slight elongation of the carbon−carbon bonds with respect to the bulk, is still observed for the core atoms in all models, suggesting that these atoms are sensitive to the surface tension given the size of the nanodiamonds. Through the examination of Figure 3, it is clear that the studied nanodiamonds do not preserve perfect tetrahedral sp^3 bond character through the entire structure as surface passivation is lost.

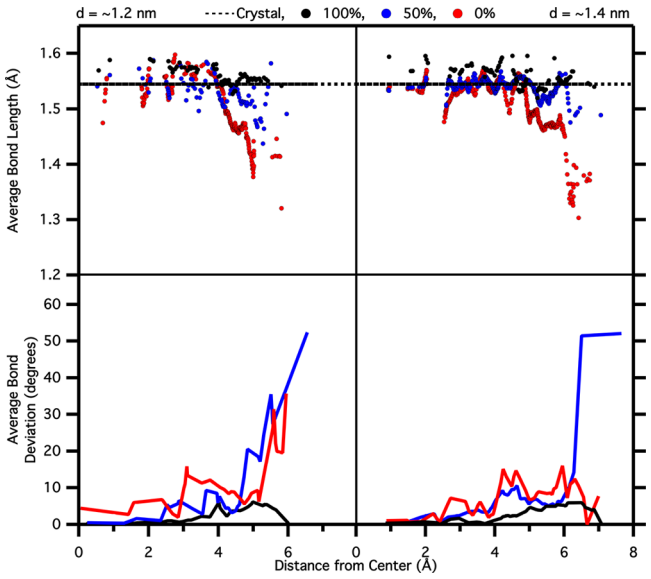

Figure 3. Bond lengths as a function of the distance from the center (top) and the root-mean-square deviation from the perfect tetrahedral bond angle of 109.5° (bottom) as a function of the distance from the center of the C_{121} diamond (left) and the C_{182} diamond (right). The dashed line marks the crystallographic bond length of 1.54 Å.

This model shows that the surface begins to undergo reconstructions when half of the hydrogens are removed. In this system, the carbon−carbon bond lengths at the surface of the nanodiamond, 5 to 6 Å from the center, decrease dramatically from ~1.5 to ~1.4 Å and from 1.5 to ~1.3 Å for the 50 and 0% surface-passivated nanodiamonds, respectively. A surface layer of ~2 Å width can be attributed to the studied systems since the bond length begins to decrease significantly ~4 Å from the center of the nanodiamond which has a total radius of ~6 Å. The bond length analysis presented here is very sensitive to the change in the carbon hybridization and therefore is very useful in highlighting the loss of sp^3 character at the surface carbon atoms. On the other hand, the bond length is less sensitive to the strained layer of sp^3 carbon (Figure 1).

To capture in a more detailed way the loss of tetrahedral character of the carbons beneath the surface of the nanodiamonds, the deviation from tetrahedral bond angles, as a function of the distance from the center of the nanodiamond, is reported in Figure 3. Examining the 1.2 nm nanodiamond, there is a dramatic loss of tetrahedral character starting ~4 Å from the center of the nanodiamond shown as a sharp increase in the deviation from the ideal tetrahedral bond angle (109.5°). This further indicates the presence of a surface layer in both the 0 and 50% cases, in agreement with bond length analysis. When the nanodiamond surface is fully passivated by hydrogens, a limited deviation of the bond angles is found, showing that the tetrahedral lattice persists through the entire structure. On the other hand, when the nanodiamond has half of the surface hydrogens, there is already a significant deviation in the bond angles starting at ~2 Å from the surface. Moreover, when all of the hydrogens have been removed there is a region ~3 Å from the surface of the nanodiamond where the bonds are still in the tetrahedral bonding regime, according to their bond lengths, but their bond angles deviate from their tetrahedral value (109.5°). This is the first evidence, in this work, of the presence of the S_2 layer (Figure 1) in nanodiamonds. The 1.2 nm nanodiamonds thus consists of a surface layer of ~3 Å in size where the sp^3 hybridization of the carbon atoms is no longer present and is further composed of both the S_1 and S_2 layers (Figure 1).

A similar result can be found for the 1.4 nm diamond (Figure 3, right panels). It is interesting that the bond angle deviation for the 1.4 nm 0% hydrogen-passivated diamond is significantly less than in the corresponding 1.2 nm nanodiamond. Upon closer inspection of the resulting optimized structures, the formation of a fullerene-like structure forming on the surface can be observed. This structure may be unable to form on the 1.2 nm nanodiamond as it may not be large enough to sustain the structure due to a larger surface tension present in smaller nanodiamonds. The dependence of this sp^2 surface formation on the size and shape of the nanodiamonds, along with the presence of graphitic/fullerene structures, has been previously observed.[2,30,31] For both 1.2 and 1.4 nm nanodiamonds, when the surface has only 50% of the original hydrogen passivation there is a significant deviation from the tetrahedral bond angle close to the surface. This observed deviation is due to the formation of noninteracting sp^2 bonds on the surface, given the uniform hydrogen distribution used in our models, that greatly distort the existing tetrahedral centers. This deviation is lessened in the 0% hydrogen cases as a more uniform graphitic structure is able to form on the surface. Given that the 1.2 and 1.4 nm nanodiamonds undergo similar surface reconstructions,

DOI: 10.1021/acs.jpcc.8b00354
J. Phys. Chem. C 2018, 122, 8573−8580

the vibrational and X-ray absorption analyses were preformed on the spectra resulting from the 1.2 nm nanodiamond.

Vibrational Analysis. Vibrational spectra, most notably Raman, can be used to identify the size and structure of nanodiamonds and their surface structure and composition.[60−63] Raman spectroscopy is sensitive to different carbon allotropes differing between various structures such as diamond, graphite, and amorphous carbon through the appearance and shapes of various bands in separate regions of the vibrational spectrum.[60−62,64] Two bands, corresponding to the breathing mode of nanodiamond and lattice carbon−carbon stretching mode energy regions, are marked in Figure 4. Note that in the

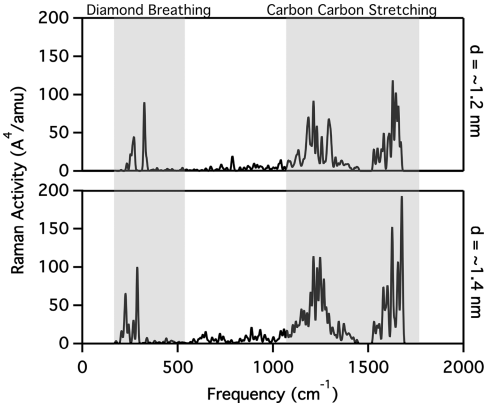

Figure 4. B3LYP/6-31G(d) Raman spectra for the 1.2- and 1.4-nm-diameter fully hydrogen passivated nanodiamonds. The high-energy carbon−hydrogen stretches (3000 cm^{-1}) are not shown. Raman activity has a 4 cm^{-1} broadening applied to generate the spectra for both plots.

lattice carbon−carbon stretching region there is an overlap with hydrogen−carbon−hydrogen bending modes responsible for the two bands. The high-energy carbon−hydrogen stretching peaks (~3000 cm^{-1}) are not of interest in this study and are thus not shown in the figure. In Figure 4 are the fully hydrogen-passivated Raman spectra for the 1.2 and 1.4 nm nanodiamonds. In particular, the measured Raman spectrum of nanodiamonds between 1200 and 1800 cm^{-1} has attracted attention given its complex nature due to several characteristic features:[63,65−67] (a) The first-order Raman mode of the cubic diamond lattice which appears broader and red-shifted (~1325 cm^{-1}) with respect to the bulk diamonds. This has been observed as the main spectral feature in this region for diamonds that have been fully passivated by hydrogen.[68,69] (b) The so-called D band at around 1400 cm^{-1} attributed to disorder and amorphous sp^2 carbons (mostly breathing motions). (c) A broad asymmetric peak between 1500 and 1800 cm^{-1} most often labeled as the G-band and assigned to the in-plane vibrations of graphitic carbon.[63,70,71] However, this peak in nanodiamonds differs from the G-band of graphitic materials in both shape and position.[72] The character of this G-band is still under debate in diamond approaching the nanosize and has either been attributed to mixed sp^2/sp^3 carbon structures[73] or referred to as a peak of sp^2 clusters,[74] without any additional explanation of their exact nature (i.e., amorphous, graphitic, etc.). There also have been attempts to attribute these peaks to carbon−carbon double-bonded pairs (C═C) within the lattice.[75,76] The lower-energy (~350 cm^{-1}) diamond breathing mode has been shown to have a size dependence, which is seen in this study through a slight red shift with increasing size of the nanodiamond, with a more in-depth investigation of this peak having been done previously.[60,61] This peak is examined as a function of decreasing surface passivation, and the Raman spectra in the energy region of interest for the three surface passivations are plotted in Figure 5. For the 100 and 50% hydrogen-passivated surfaces,

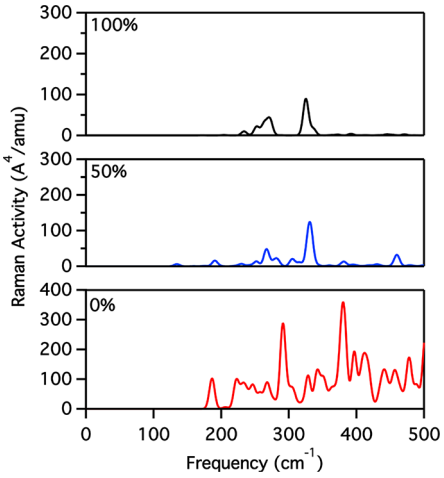

Figure 5. Diamond lattice breathing region of the B3LYP/6-31G(d) Raman spectra for the 100, 50, and 0% in black, blue, and red, respectively. Raman activity has had a 4 cm^{-1} broadening applied to generate the spectra for all three plots.

this peak is shown not to change drastically; however, with the removal of all of the surface passivation, this band grows in intensity.

Examining the lattice carbon−carbon stretching region (~1300 cm^{-1}) in Figure 4, two separate bands can be identified. These bands are due to hydrogen−carbon−hydrogen bending modes overlapping with carbon−carbon stretching modes. The obscuring of the carbon−carbon stretches has been noted in previous vibrational studies of nanodiamonds and has been addressed by artificially increasing the mass of the hydrogen atoms (to 100 amu) so as to shift their response away from the carbon−carbon stretching energy regions.[60,64] The Raman spectra with heavy hydrogen for the 100, 50, and 0% surface-passivated surfaces are plotted in Figure 6. In the case where the nanodiamond has 100% surface hydrogen passivation, a band is seen at 1318 cm^{-1}. This band is commonly referred to as the Raman diamond band and is seen in diamond samples as a sharp peak, but as previously mentioned, at the nanoscale the band has been observed to decrease in intensity and a 10−20 cm^{-1} red shift of this peak (1325 cm^{-1})[66,68,69] is observed due to the size constraints of our system. Thus, the calculated value of 1318 cm^{-1} shows good agreement with the experiments. When part, or all, of the surface hydrogen is removed, this band decreases in intensity and broadens in agreement with the Raman spectrum of nanodiamonds.[63,65−67] A so-called D-band at around 1400 cm^{-1} starts to arise and is attributed to disorder and amorphous sp^2 carbons (mostly breathing motions), as can be inferred from Figure 4. The D-band appears in both the 50 and 0% models because of the presence of amorphous sp^2 carbon giving rise to mixed sp^2 and sp^3 carbon ring-breathing motions (Table S2), in agreement with previous studies.[63] In our work concerning the G-band region, the 0% model shows a red-shifted value for this band at 1564 cm^{-1}. Since the 0% coverage

DOI: 10.1021/acs.jpcc.8b00354
J. Phys. Chem. C 2018, 122, 8573−8580

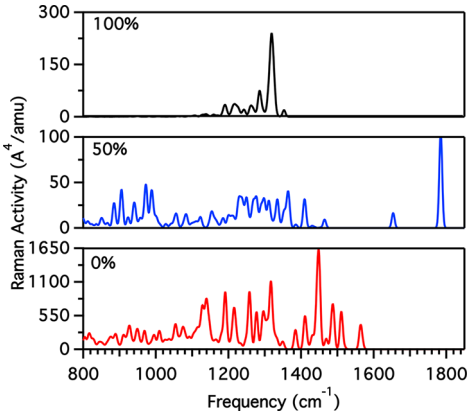

Figure 6. B3LYP/6-31G(d) Raman spectra of the diamond lattice carbon−carbon stretching region (800−1650 cm^{-1}) for the 0, 50, and 100% nanodiamonds (shown in red, blue, and black, respectively). A carbon−carbon triple-bonding peak is not shown at 2100 cm^1 in the 0% hydrogen nanodiamond spectrum. Raman activity has a 4 cm^{-1} broadening applied to generate the spectra for all three plots.

cannot support a truly graphitic structure on the surface but rather sp^2 rings, mixed sp^2 rings, mixed sp^2/sp^3 rings, and chains causing softer vibrational modes to appear (Table S2), this is consistent with the amorphous sp^2, or disordered graphitic layer, interpretation of this peak for nanostructures.[63,73,74] The 50% model shows instead no vibrational modes between ∼1470 and ∼1650 cm^{-1} as the surface is forming more amorphous and isolated sp^2 features given the modeling strategy of uniformly passivating the surface with hydrogen. In addition, two isolated peaks are observed in Figure S3 at ∼1530 and ∼1727 cm^{-1} (values using regular hydrogen mass are reported since these two peaks show greater sensitivity to the hydrogen mass in contrast to those below ∼1450 cm^{-1}) for the 50% model due to isolated sp^2 moieties that are supported by this model. The peak at ∼1530 is ascribed to a breathing motion of a four-membered carbon cage (Table S2) which resembles previously performed calculations and experiments on caged structures of similar size (∼1580 cm^{-1}).[77,78] The ∼1727 cm^{-1} feature is due to isolated C═C double-bond stretching and H−C═C−H bending mixed modes which happen to be blue-shifted from the experimental Raman response for the C═C stretchting motion (1622 cm^{-1}).[79] These shifts may be due to the harmonic treatment used in our work. However, in synthetic or natural diamond, these regions might contain several modes from surface moieties such as carboxyl and hydroxyl groups, making the overall vibrational analysis even more complex.[67]

As the surface of the nanodiamond loses hydrogen atoms and begins to form graphitic structures, low-energy breathing modes of the diamonds increase in their spectral response, and additional bands are observed in the Raman spectra. For diamonds synthesized through detonations or in a multianvil press, however, significant differences in the Raman cross section of different surface moieties overshadow and obscure each other. However, diamonds synthesized with a laser-heated diamond anvil cell likely have the lowest degree of surface hydrogen or oxygen bonding due to the use of chemically inert noble gases (neon, argon) as nearly hydrostatic pressure media. A more specific analytical method is thus required to characterize these nanodiamonds.

X-ray Carbon K-Edge. X-ray absorption spectroscopy is an ideal spectroscopic technique because it is highly sensitive to both elemental composition and local changes in the molecular structures as electronic transitions from atomic core electrons to weakly bound states are involved.[50] In nanodiamond, XAS has been used to characterize heteroatomic dopants and study surface reconstruction.[23,80] In this particular study, the different surface reconstructions can be probed by the different transitions involving carbon 1s core electrons and the electronic states involving the different antibonding molecular orbitals lying on the surface. To provide insights into the experimental X-ray data,[13,23] theoretical calculations are required to correlate the observed transitions with the molecular orbitals involved. The excited-state orbitals involved in these transitions for nanodiamond typically have σ^* properties if located on sp^3 carbons or can be π^* and σ^* if they are centered on sp^2 carbons, when these are present. Thus, electronic excitations in the carbon K-edge, which involves transitions from carbon 1s orbitals to virtual orbitals, were computed and analyzed. Once these transitions are computed, determining if the spatial extent of the virtual molecular orbitals involved in the transition exhibits π^* or σ^* character enables a direct correlation between the surface structure and X-ray spectral features. The resulting carbon K-edge X-ray absorption spectra from the 1.2 nm nanodiamond with 100, 50, and 0% hydrogen passivation are shown in Figure 7, and the corresponding computed transitions of interest are reported in the Supporting Information.

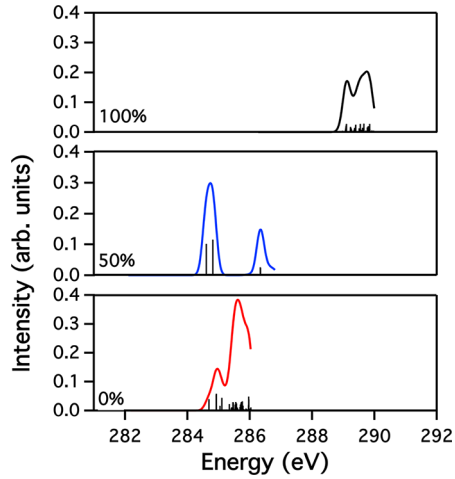

Figure 7. LR-B3LYP/6-31G(d) XAS for the optimized C_{121} diamond with 100, 50, and 0% surface passivation in red, green, and blue, respectively. Gaussian broadening has been applied to the individual transitions labeled with black lines to form the spectrum with a full width at half-maximum value of 0.12 eV along with a uniform shift of 12 eV to align the computed results with the experiments. For the 100% diamond, 35 unconverged states of the calculated 272 states were pruned, along with 14 unconverged states of the 121 states calculated for the 50% diamond.

When the surface is fully passivated, the first transition in the carbon K-edge region is localized at 289 eV and is of the type carbon 1s → σ^*, determined through studying the molecular orbitals (plotted in Figure 8). Upon the loss of half of the surface passivation, the surface forms sp^2-hybridized carbons. This rearrangement alters the calculated X-ray spectrum so that transitions at around 285 eV arise, which are red-shifted from the sp^3 transition in pure diamond at 289 eV by approximately 4 eV, indicating that the presence of sp^2 carbon is at least partially responsible for the experimentally observed pre-edge

DOI: 10.1021/acs.jpcc.8b00354
J. Phys. Chem. C 2018, 122, 8573−8580

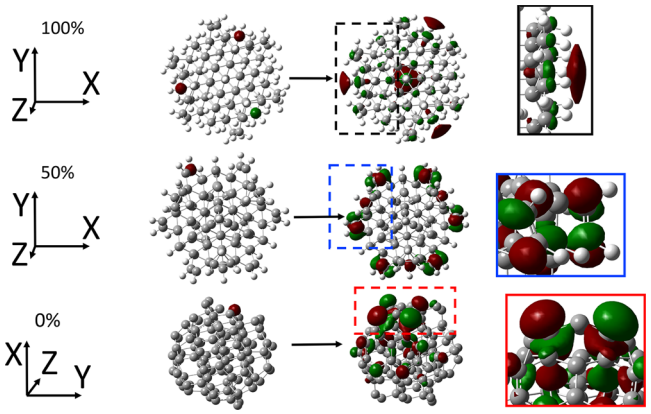

Figure 8. B3LYP/6-31G(d) molecular orbitals for the first transition in the carbon K-edge shown in Figure 7 for the 100, 50, and 0% nanodiamonds, plotted with an isovalue of 0.025.

feature in synthesized nanodiamond.[2,26,81] The pre-edge features are due to carbon 1s → π^* (shown in Figure 8). For the 0% nanodiamond, the first peak is again red-shifted from the 100% surface-passivated nanodiamond by about 4 eV to 285 eV and the excitations are still carbon 1s → π^* (shown in Figure 8), similar to that of the 50% surface-passivated nanodiamond. The appearance of transitions that are red-shifted upon the loss of the surface passivation indicates that the shifted peak is dependent on the surface hybridization of the nanodiamond. In the case of both 0 and 50% surface passivations, a second pre-edge feature arises (at ∼285.5 eV and at ∼286.7 eV for 0 and 50%, respectively) which is still due to carbon 1s →π^* transitions, with the molecular orbitals involved plotted in the Supporting Information (Figure S2). These features differ from the first-appearing features (at ∼285 eV) only in the spacial localization, with respect to the surface of the nanodiamond, of the virtual (arriving) orbitals mostly involved in the corresponding transitions. Therefore, as the surface of the nanodiamond becomes increasingly graphitized, through either heating or chemical treatment, an increase in this pre-edge feature is expected, proportional to the amount of sp^2 carbon.

CONCLUSIONS

In this work, several nanodiamond nanocrystals were modeled and examined in order to determine how different surface layouts can affect the crystallinity of the diamonds as the systems approach the nanoscale. The nanodiamonds were found to form a ∼ 3 Å surface composed of a layer of sp^2-hybridized carbon and a strained layer of sp^3 carbon, while the core of the nanodiamond remained in an sp^3 tetrahedral lattice to form the structure pictured in Figure 1 as hydrogen atoms were removed from the surface. The spectroscopic fingerprints of nanodiamond in both the vibrational and X-ray absorption spectra were therefore analyzed to find evidence of this rearrangement. This rearrangement showed a response in the vibrational spectra as the appearance of sp^2 stretching vibrations in the Raman G-band (∼1500 cm^{-1}) and a broadening of the Raman diamond band (1330 cm^{-1}). The significant sp^2 character present in unpassivated nanodiamonds has the effect of changing the X-ray absorption spectrum to show carbon 1s to π^* electronic transitions, absent in the calculated spectra for the fully passivated systems. Thus, surface rearrangement is responsible for observed pre-edge features (5 eV lower in energy peak) of the X-ray absorption carbon K-edge spectra of nanodiamonds and was correlated to the carbon 1s to π^* electronic transitions.

ASSOCIATED CONTENT

Supporting Information

The Supporting Information is available free of charge on the ACS Publications website at DOI: 10.1021/acs.jpcc.8b00354.

Additional analyses of vibrational signals and electronic transitions (PDF)

AUTHOR INFORMATION

Corresponding Author

*E-mail: xsli@uw.edu.

ORCID

Alessio Petrone: 0000-0003-2232-9934
Joseph M. Kasper: 0000-0002-3840-484X
Xiaosong Li: 0000-0001-7341-6240

Author Contributions

§These authors contributed equally to this work

Notes

The authors declare no competing financial interest.

ACKNOWLEDGMENTS

The development of the energy-specific TDDFT method for computing XAS spectra was supported by the NSF (CHE-1565520 to XL). The study of defects in nanodiamond was supported by the University of Washington Molecular Engineering Materials Center (DMR-1719797) and the NSF (CHE-1464497 to X.L. and NSF-CAREER 1555007 to P.J.P.). This work was facilitated though the use of advanced computational, storage, and networking infrastructure provided by the Hyak supercomputer system and funded by the STF at the University of Washington and the National Science Foundation (MRI-1624430).

REFERENCES

(1) Holt, K. Diamond at the Nanoscale: Applications of Diamond Nanoparticles from Cellular Biomarkers to Quantum Computing. *Philos. Trans. R. Soc., A* **2007**, *365*, 2845−2861.

(2) Galli, G. In *Computer-Based Modeling of Novel Carbon Systems and Their Properties: Beyond Nanotubes*; Colombo, L., Fasolino, A., Eds.; Springer: Dordrecht, The Netherlands, 2010; pp 37−56.

(3) Mortet, V.; Zhang, L.; Eckert, M.; D'Haen, J.; Soltani, A.; Moreau, M.; Troadec, D.; Neyts, E.; Jaeger, J.-C. D.; Verbeeck, J.; et al. Grain Size Tuning of Nanocrystalline Chemical Vapor Deposited Diamond by Continuous Electrical Bias Growth: Experimental and Theoretical Study. *Phys. Status Solidi A* **2012**, *209*, 1675−1682.

(4) Pezzagna, S.; Rogalla, D.; Wildanger, D.; Meijer, J.; Zaitsev, A. Creation and Nature of Optical Centres in Diamond for Single-Photon Emission-Overview and Critical Remarks. *New J. Phys.* **2011**, *13*, 035024.

(5) Dolde, F.; Doherty, M. W.; Michl, J.; Jakobi, I.; Naydenov, B.; Pezzagna, S.; Meijer, J.; Neumann, P.; Jelezko, F.; Manson, N. B.; et al. Nanoscale Detection of a Single Fundamental Charge in Ambient Conditions Using the NV^- Center in Diamond. *Phys. Rev. Lett.* **2014**, *112*, 097603.

(6) Balasubramanian, G.; Chan, I.; Kolesov, R.; Al-Hmoud, M.; Tisler, J.; Shin, C.; Kim, C.; Wojcik, A.; Hemmer, P.; Krueger, A.; et al. Nanoscale Imaging Magnetometry with Diamond Spins Under Ambient Conditions. *Nature* **2008**, *455*, 648−651.

DOI: 10.1021/acs.jpcc.8b00354
J. Phys. Chem. C 2018, 122, 8573−8580

(7) Bawendi, M. G.; Steigerwald, M. L.; Brus, L. E. The Quantum Mechanics of Larger Semiconductor Clusters ("Quantum Dots"). *Annu. Rev. Phys. Chem.* **1990**, *41*, 477−496.
(8) Karin, T.; Dunham, S.; Fu, K.-M. Alignment of the Diamond Nitrogen Vacancy Center by Strain Engineering. *Appl. Phys. Lett.* **2014**, *105*, 053106.
(9) Drake, M.; Scott, E.; Reimer, J. Influence of Magnetic Field Alignment and Defect Concentration on Nitrogen-Vacancy Polarization in Diamond. *New J. Phys.* **2016**, *18*, 013011.
(10) Levinshteĭn, M. E.; Rumyantsev, S. L.; Shur, M. *Handbook Series on Semiconductor Parameters: Si, Ge, C (Diamond), GaAs, GaP, GaSb, InAs, InP, InSb*; World Scientific Publishing: Singapore, 1996.
(11) Petrone, A.; Goings, J. J.; Li, X. Quantum Confinement Effects on Optical Transitions in Nanodiamonds Containing Nitrogen Vacancies. *Phys. Rev. B: Condens. Matter Mater. Phys.* **2016**, *94*, 165402.
(12) Gali, A.; Maze, J. R. *Ab Initio* Study of the Split Silicon-Vacancy Defect in Diamond: Electronic Structure and Related Properties. *Phys. Rev. B: Condens. Matter Mater. Phys.* **2013**, *88*, 235205.
(13) Pauzauskie, P. J.; Crowhurst, J. C.; Worsley, M. A.; Laurence, T. A.; Kilcoyne, A. L. D.; Wang, Y.; Willey, T. M.; Visbeck, K. S.; Fakra, S. C.; Evans, W. J.; et al. Synthesis and Characterization of a Nanocrystalline Diamond Aerogel. *Proc. Natl. Acad. Sci. U. S. A.* **2011**, *108*, 8550−8553.
(14) Chelikowsky, J. R.; Alemany, M. M. G.; Chan, T.-L.; Dalpian, G. M. Computational Studies of Doped Nanostructures. *Rep. Prog. Phys.* **2011**, *74*, 046501.
(15) Beaulac, R.; Ochsenbein, S. T.; Gamelin, D. R. In *Semiconductor Quantum Dots*, 2nd ed.; Klimov, V. I., Ed.; CRC Press, 2010; Chapter 11, p 397.
(16) Canham, L. Gaining Light from Silicon. *Nature* **2000**, *408*, 411−412.
(17) Chelikowsky, J. Silicon in All Its Forms. *MRS Bull.* **2002**, *27*, 951.
(18) Chelikowsky, J. Why Silicon is the Benchmark. Mater. *Mater. Today* **2002**, *5*, 64.
(19) Chelikowsky, J. R.; Cohen, M. L. Electronic Structure of GaAs. *Phys. Rev. Lett.* **1974**, *32*, 674−677.
(20) Kittel, C.; McEuen, P. *Introduction to Solid State Physics*; Wiley: New York, 1976; Vol. *8*.
(21) Ashcroft, N.; Mermin, N. *Solid State Physics*; Saunders College: Philadelphia, PA, 1976.
(22) Brus, L. E. Electron-Electron and Electron-Hole Interactions in Small Semiconductor Crystallites: The Size Dependence of the Lowest Excited Electronic State. *J. Chem. Phys.* **1984**, *80*, 4403−4409.
(23) Raty, J.-Y.; Galli, G.; Bostedt, C.; van Buuren, T. W.; Terminello, L. J. Quantum Confinement and Fullerenelike Surface Reconstructions in Nanodiamonds. *Phys. Rev. Lett.* **2003**, *90*, 037401.
(24) Chang, S. L.; Barnard, A. S.; Dwyer, C.; Boothroyd, C. B.; Hocking, R. K.; Ōsawa, E.; Nicholls, R. J. Counting Vacancies and Nitrogen-Vacancy Centers in Detonation Nanodiamond. *Nanoscale* **2016**, *8*, 10548−10552.
(25) Palosz, B.; Pantea, C.; Grzanka, E.; Stelmakh, S.; Proffen, T.; Zerda, T. W.; Palosz, W. Investigation of Relaxation of Nanodiamond Surface in Real and Reciprocal Spaces. *Diamond Relat. Mater.* **2006**, *15*, 1813−1817.
(26) Hamon, A.-L.; Verbeeck, J.; Schryvers, D.; Benedikt, J.; vd Sanden, R. M. ELNES Study of Carbon K-edge Spectra of Plasma Deposited Carbon Films. *J. Mater. Chem.* **2004**, *14*, 2030−2035.
(27) Barnard, A. S.; Sternberg, M. Crystallinity and Surface Electrostatics of Diamond Nanocrystals. *J. Mater. Chem.* **2007**, *17*, 4811−4819.
(28) Lai, L.; Barnard, A. S. Surface Phase Diagram and Thermodynamic Stability of Functionalisation of Nanodiamonds. *J. Mater. Chem.* **2012**, *22*, 16774−16780.
(29) Lai, L.; Barnard, A. S. Site-Dependent Atomic and Molecular Affinities of Hydrocarbons, Amines, and Thiols on Diamond Nanoparticles. *Nanoscale* **2016**, *8*, 7899−7905.
(30) Chang, S. L.; Dwyer, C.; Osawa, E.; Barnard, A. S. Size Dependent Surface Reconstruction in Detonation Nanodiamonds. *Nanoscale Horiz.* **2018**, *3*, 213−217.
(31) Barnard, A. S.; Russo, S. P.; Snook, I. K. *Ab initio* Modeling of B and N in C^{29} and C^{29} H^{24} Nanodiamond. *J. Chem. Phys.* **2003**, *118*, 10725−10728.
(32) Liang, W.; Fischer, S. A.; Frisch, M. J.; Li, X. Energy-Specific Linear Response TDHF/TDDFT for Calculating High-Energy Excited States. *J. Chem. Theory Comput.* **2011**, *7*, 3540−3547.
(33) Lestrange, P. J.; Nguyen, P. D.; Li, X. Calibration of Energy-Specific TDDFT for Modeling K-edge XAS Spectra of Light Elements. *J. Chem. Theory Comput.* **2015**, *11*, 2994−2999.
(34) Van Beeumen, R.; Williams-Young, D. B.; Kasper, J. M.; Yang, C.; Ng, E. G.; Li, X. A Model Order Reduction Algorithm for Estimating the Absorption Spectrum. *J. Chem. Theory Comput.* **2017**, *13*, 4950−4961.
(35) Guido, C. A.; Knecht, S.; Kongsted, J.; Mennucci, B. Benchmarking Time-Dependent Density Functional Theory for Excited State Geometries of Organic Molecules in Gas-Phase and in Solution. *J. Chem. Theory Comput.* **2013**, *9*, 2209−2220.
(36) Badaeva, E.; Isborn, C. M.; Feng, Y.; Ochsenbein, S. T.; Gamelin, D. R.; Li, X. Theoretical Characterization of Electronic Transitions in Co^{2+}- and Mn^{2+} -Doped ZnO Nanocrystals. *J. Phys. Chem. C* **2009**, *113*, 8710−8717.
(37) Beaulac, R.; Feng, Y.; May, J. W.; Badaeva, E.; Gamelin, D. R.; Li, X. Orbital Pathways for Mn^{2+}-carrier *Sp*−*d* Exchange in Diluted Magnetic Semiconductor Quantum Dots. *Phys. Rev. B: Condens. Matter Mater. Phys.* **2011**, *84*, 195324.
(38) Gary, D. C.; Petrone, A.; Li, X.; Cossairt, B. M. Investigating the Role of Amine in InP Nanocrystal Synthesis: Destabilizing Cluster Intermediates by Z-type Ligand Displacement. *Chem. Commun.* **2017**, *53*, 161−164.
(39) Chong, E. Q.; Lingerfelt, D. B.; Petrone, A.; Li, X. Classical or Quantum? A Computational Study of Small Ion Diffusion in II−VI Semiconductor Quantum Dots. *J. Phys. Chem. C* **2016**, *120*, 19434−19441.
(40) Stein, J. L.; Steimle, M. I.; Terban, M. W.; Petrone, A.; Billinge, S. J.; Li, X.; Cossairt, B. M. Cation Exchange Induced Transformation of InP Magic-Sized Clusters. *Chem. Mater.* **2017**, *29*, 7984−7992.
(41) Wong, M. W. Vibrational Frequency Prediction using Density Functional Theory. *Chem. Phys. Lett.* **1996**, *256*, 391−399.
(42) Barone, V.; Bloino, J.; Biczysko, M. Validation of the DFT/N06D Computational Model on the Magnetic, Vibrational, and Electronic Properites of Vinyl Radical. *Phys. Chem. Chem. Phys.* **2010**, *12*, 1092−1101.
(43) Petrone, A.; Lingerfelt, D. B.; Williams-Young, D. B.; Li, X. *Ab Initio* Transient Vibrational Spectral Analysis. *J. Phys. Chem. Lett.* **2016**, *7*, 4501−4508.
(44) Donati, G.; Lingerfelt, D. B.; Petrone, A.; Rega, N.; Li, X. Watching" Polaron Pair Formation from First-Principles Electron−Nuclear Dynamics. *J. Phys. Chem. A* **2016**, *120*, 7255−7261.
(45) Lingerfelt, D. B.; Williams-Young, D. B.; Petrone, A.; Li, X. Direct *Ab Initio* (Meta-)Surface-Hopping Dynamics. *J. Chem. Theory Comput.* **2016**, *12*, 935−945.
(46) Arnault, J.-C.; Petit, T.; Girard, H.; Chavanne, A.; Gesset, C.; Sennour, M.; Chaigneau, M. Surface Chemical Modifications and Surface Reactivity of Nanodiamonds Hydrogenated by CVD Plasma. *Phys. Chem. Chem. Phys.* **2011**, *13*, 11481−11487.
(47) John, P.; Stoikou, M. D. Hydrogen Plasma Interaction with (100) Diamond Surfaces. *Phys. Chem. Chem. Phys.* **2011**, *13*, 11503−11510.
(48) Mochalin, V. N.; Shenderova, O.; Ho, D.; Gogotsi, Y. The Properties and Applications of Nanodiamonds. *Nat. Nanotechnol.* **2012**, *7*, 11−23.
(49) Mandal, M.; Haso, F.; Liu, T.; Fei, Y.; Landskron, K. Size Tunable Synthesis of Solution Processable Diamond Nanocrystals. *Chem. Commun.* **2014**, *50*, 11307−11310.
(50) Stöhr, J. *NEXAFS Spectroscopy*; Springer-Verlag: Berlin, 2003.

DOI: 10.1021/acs.jpcc.8b00354
J. Phys. Chem. C 2018, 122, 8573−8580

(51) Takahashi, K.; Yoshikawa, A.; Sandhu, A. *Wide Bandgap Semiconductors: Fundamental Properties and Modern Photonic and Electronic Devices*; Springer: New York, 2007.
(52) Frisch, M. J.; Trucks, G. W.; Schlegel, H. B.; Scuseria, G. E.; Robb, M. A.; Cheeseman, J. R.; Scalmani, G.; Barone, V.; Petersson, G. A.; Nakatsuji, H. et al. *Gaussian 16*, Revision A.03; Gaussian Inc.: Wallingford, CT, 2016.
(53) Becke, A. D. Density-Functional Thermochemistry. III. The Role of Exact Exchange. *J. Chem. Phys.* **1993**, *98*, 5648.
(54) Lee, C.; Yang, W.; Parr, R. G. Development of the Colle-Salvetti Correlation-Energy Formula into a Functional of the Electron Density. *Phys. Rev. B: Condens. Matter Mater. Phys.* **1988**, *37*, 785.
(55) Miehlich, B.; Savin, A.; Stoll, H.; Preuss, H. Results Obtained with the Correlation Energy Density Functionals of Becke and Lee, Yang and Parr. *Chem. Phys. Lett.* **1989**, *157*, 200−206.
(56) Li, X.; Frisch, M. J. Energy-Represented Direct Inversion in the Iterative Subspace Within a Hybrid Geometry Optimization Method. *J. Chem. Theory Comput.* **2006**, *2*, 835−839.
(57) Casida, M. E. In *Recent Advances in Density Functional Methods: (Part I)*; Chong, D. P., Ed.; World Scientific Publishing: Singapore, 1995; Vol. *1*; pp 155−193.
(58) Dreuw, A.; Head-Gordon, M. Single-reference ab initio methods for the calculation of excited states of large molecules. *Chem. Rev.* **2005**, *105*, 4009−4037.
(59) Stratmann, R. E.; Scuseria, G. E.; Frisch, M. J. An Efficient Implementation of Time-Dependent Density-Functional Theory for the Calculation of Excitation Energies of Large Molecules. *J. Chem. Phys.* **1998**, *109*, 8218−8224.
(60) Filik, J.; Harvey, J.; Allan, N.; May, P. Raman Spectroscopy of Nanocrystalline Diamond: An *ab initio* Approach. *Phys. Rev. B: Condens. Matter Mater. Phys.* **2006**, *74*, 035423.
(61) Li, W.; Irle, S.; Witek, H. A. Convergence in the Evolution of Nanodiamond Raman Spectra with Particle Size: A Theoretical Investigation. *ACS Nano* **2010**, *4*, 4475−4486.
(62) Prawer, S.; Rosenblum, I.; Orwa, J.; Adler, J. Identification of the Point Defects in Diamond as Measured by Raman Spectroscopy: Comparison Between Experiment and Computation. *Chem. Phys. Lett.* **2004**, *390*, 458−461.
(63) Ferrari, A. C.; Robertson, J. Raman Spectroscopy of Amorphous, Nanostructured, Diamond−Like Carbon, and Nanodiamond. *Philos. Trans. R. Soc., A* **2004**, *362*, 2477−2512.
(64) Negri, F.; Castiglioni, C.; Tommasini, M.; Zerbi, G. A Computational Study of the Raman Spectra of Large Polycyclic Aromatic Hydrocarbons: Toward Molecularly Defined Subunits of Graphite. *J. Phys. Chem. A* **2002**, *106*, 3306−3317.
(65) Popov, M.; Churkin, V.; Kirichenko, A.; Denisov, V.; Ovsyannikov, D.; Kulnitskiy, B.; Perezhogin, I.; Aksenenkov, V.; Blank, V. Raman Spectra and Bulk Modulus of Nanodiamond in a Size Interval of 2−5 nm. *Nanoscale Res. Lett.* **2017**, *12*, 561.
(66) Mochalin, V.; Osswald, S.; Gogotsi, Y. Contribution of Functional Groups to the Raman Spectrum of Nanodiamond Powders. *Chem. Mater.* **2009**, *21*, 273−279.
(67) Cebik, J.; McDonough, J. K.; Peerally, F.; Medrano, R.; Neitzel, I.; Gogotsi, Y.; Osswald, S. Raman Spectroscopy Study of the Nanodiamond to Carbon Onion Transformation. *Nanotechnology* **2013**, *24*, 205703.
(68) Ando, T.; Ishii, M.; Kamo, M.; Sato, Y. Diffuse Reflectance Infrared Fourier-Transform Study of the Plasma Hydrogenation of Diamond Surfaces. *J. Chem. Soc., Faraday Trans.* **1993**, *89*, 1383−1386.
(69) Stehlik, S.; Varga, M.; Ledinsky, M.; Jirasek, V.; Artemenko, A.; Kozak, H.; Ondic, L.; Skakalova, V.; Argentero, G.; Pennycook, T.; et al. Size and Purity Control of HPHT Nanodiamonds Down to 1 nm. *J. Phys. Chem. C* **2015**, *119*, 27708−27720.
(70) Birrell, J.; Gerbi, J.; Auciello, O.; Gibson, J.; Johnson, J.; Carlisle, J. Interpretation of the Raman Spectra of Ultrananocrystalline Diamond. *Diamond Relat. Mater.* **2005**, *14*, 86−92.
(71) Ferrari, A. C.; Robertson, J. Origin of the 1150-cm^{-1} Raman Mode in Nanocrystalline Diamond. *Phys. Rev. B: Condens. Matter Mater. Phys.* **2001**, *63*, 121405.
(72) Reich, S.; Thomsen, C. Raman Spectroscopy of Graphite. *Philos. Trans. R. Soc., A* **2004**, *362*, 2271−2288.
(73) Mykhaylyk, O. O.; Solonin, Y. M. Transformation of Nanodiamond into Carbon Onions: A Comparative Study by High-Resolution Transmission Electron Microscopy, Electron Energy-Loss Spectroscopy, X-Ray Diffraction, Small-Angle X-Ray Scattering, and Ulraviolet Raman Spectroscopy. *J. Appl. Phys.* **2005**, *97*, 074302.
(74) Yoshikawa, M.; Mori, Y.; Obata, H.; Maegawa, M.; Katagiri, G.; Ishida, H.; Ishitani, A. Raman Scattering from Nanometer-Sized Diamond. *Appl. Phys. Lett.* **1995**, *67*, 694−696.
(75) Prawer, S.; Nemanich, R. Raman Spectroscopy of Diamond and Doped Diamond. *Philos. Trans. R. Soc., A* **2004**, *362*, 2537−2565.
(76) Prawer, S.; Nugent, K.; Jamieson, D.; Orwa, J.; Bursill, L. A.; Peng, J. The Raman Spectrum of Nanocrystalline Diamond. *Chem. Phys. Lett.* **2000**, *332*, 93−97.
(77) Andes Hess, B., Jr.; Schaad, L. J. *Ab Initio* Second-Order Möller-Plesset Calculation of the Vibrational Spectrum of Tetrahedrane. *J. Am. Chem. Soc.* **1985**, *107*, 865−866.
(78) Masamune, S.; Souto-Bachiller, F. A.; Machiguchi, T.; Bertie, J. E. Cyclobutadiene Is Not Square. *J. Am. Chem. Soc.* **1978**, *100*, 4889−4891.
(79) Shimanouchi, T. *Tables of Molecular Vibrational Frequencies: Consolidated Volume I*; U.S. National Bureau of Standards: Washington, DC, 1972.
(80) Castrucci, P.; Scarselli, M.; Crescenzi, M. D.; Khakani, M. A. E.; Rosei, F. Probing the Electronic Structure of Carbon Nanotubes by Nanoscale Spectroscopy. *Nanoscale* **2010**, *2*, 1611−1625.
(81) Papworth, A. J.; Kiely, C.; Burden, A.; Silva, S.; Amaratunga, G. Electron-Energy-Loss Spectroscopy Characterization of the sp^2 Bonding Fraction within Carbon Thin Films. *Phys. Rev. B: Condens. Matter Mater. Phys.* **2000**, *62*, 12628−12631.

DOI: 10.1021/acs.jpcc.8b00354
J. Phys. Chem. C 2018, 122, 8573−8580